PAPER

Check for updates

Enhanced removal of phosphate from aqueous solutions by MgAl-LDH impregnated with LaFeO₃

Abdelazeem S. Eltaweil, [ID] *[ab] Hossam A. Mohamed*[b] and Gehan M. El-Subruiti[b]

Water eutrophication, driven by excessive phosphate levels, represents a major environmental challenge. Conventional adsorbents exhibit limitations in efficiently removing phosphate ions (P-ions) from aqueous solutions. This study aimed to develop an MgAl-LDH/LaFeO₃ composite as a more effective adsorbent for P-ion removal. The prepared composite was characterized using various techniques, including XRD, FTIR, SEM, and XPS, to verify its successful fabrication. Zeta potential analysis determined the surface charge to be +32.1 mV at pH 2. Results demonstrated a synergistic effect between LaFeO₃ and MgAl-LDH, which significantly enhanced the composite's overall removal efficiency. The optimal pH for P-ion removal was found to be 2, with a high selectivity for P-ions. Phosphate ion removal followed second-order kinetics and fitted well with both Freundlich and Langmuir isotherms, exhibiting a maximum adsorption capacity of 833.3 mg-P per g. Analyses after adsorption clarified that there was a combination of physical and chemical interactions, including electrostatic attraction, complexation, ion exchange, and ligand exchange, in the removal mechanism. Reusability test showed that the composite maintained over 88% removal efficiency after five cycles, confirming its stability and applicability. These findings highlight the superior adsorption capacity of the MgAl-LDH/LaFeO₃ composite, offering an efficient solution for mitigating phosphate pollution.

1. Introduction

Water is essential for life and is crucial for agriculture, drinking, and industrial purposes. Water treatment processes play a vital role in ensuring that water and wastewater are clean and safe for use.[1] These processes involve physical, chemical, and biological methods to remove harmful solids and organic materials.[2] Phosphate $(PO_4)^{3-}$ is a crucial component in many industrial processes and agricultural activities. Approximately 90% of the globally produced phosphate is utilized in fertilizers, industrial products, including detergents and food and beverages, and metallurgy.[3] However, the excessive discharge of dissolved phosphate from industrial, agricultural, and domestic sources into water bodies contributes to water eutrophication.[3] This phenomenon causes substantial economic losses, promotes algal blooms, and disrupts the biological balance of aquatic ecosystems. To maintain clean and safe water, controlling the concentration of phosphorus-containing ions has become essential. Despite the use of chemical, physical, and biological methods to eliminate phosphate ions, adsorption remains a preferable technique due to its efficiency, simplicity, and sensitivity to toxic contaminants.

To date, various adsorbents, including activated carbon, polymers, metal-based composites, and biochar, have been utilized for phosphate removal.[3] Among these, layered double hydroxide (LDH) materials, a type of anionic clay, have gained significant attention due to their versatile applications in catalysis, sensing, drug delivery, and adsorption.[2,4,5] LDHs are highly efficient in adsorbing different types of contaminants, boasting a remarkable ion-exchange capacity and exceptional performance in removing hazardous elements from wastewater. Their unique structural and chemical properties make LDHs highly promising materials for phosphate removal.[6] LDHs consist of positively charged brucite-like layers intercalated with anions that maintain charge balance, offering a substantial interlayer surface for accommodating and adsorbing various anionic contaminants, including phosphate.[7,8] Numerous studies have demonstrated the efficacy of LDHs in water treatment applications, with phosphate adsorption capacities varying based on the metal ions incorporated into the LDH structure. For example, Ca–La LDHs have shown exceptional adsorption capacities of up to 194.04 mg P per g, outperforming other LDHs due to their selective chemical adsorption, ion exchange, and inner-sphere complexation.[9] Similarly, Zn–Al LDHs exhibit high phosphate removal efficiencies, such as 116.07 mg P per g, while biochar-enhanced MgAl–LDHs have demonstrated superior selectivity and regeneration potential for real wastewater treatment.[10] Modified LDHs, such as La-doped LDHs, further enhance the adsorption performance by

[a]Department of Engineering, Faculty of Technology and Engineering, University of Technology and Applied Sciences, Sultanate of Oman

[b]Chemistry Department, Faculty of Science, Alexandria University, Alexandria, Egypt. E-mail: abdelazeemeltaweil@alexu.edu.eg; hossam.ali_pg@alexu.edu.eg

increasing the adsorption sites and improving the resistance to pH variations and competing anions.[11] However, there are challenges that still need to be improved, particularly concerning the selectivity, stability of LDHs under varying pH conditions, and the nano-scale nature of these materials, which complicates separation. To address these limitations, doping LDHs with lanthanum-based materials for example could enhance their selectivity towards phosphate ions. Furthermore, incorporating materials with magnetic property can greatly enhance their separation.

Lanthanum (La), in its metallic form, is well-known for its effectiveness as an adsorbent for removing phosphate from contaminated water. Its cationic form, La^{3+}, exhibits a high affinity for bonding with phosphate ions (P-ions) by drawing oxygen-donor atoms from phosphate through an anion-ligand mechanism. Additionally, La can form a La–phosphate (La–PO_4) complex even with trace amounts of phosphate.[12,13] La-based adsorbents, particularly lanthanum ferrite ($LaFeO_3$), a type of perovskite oxide, have attracted significant interest due to their diverse and advantageous physicochemical properties for the adsorption of water pollutants.[14,15]

The objectives of this study are to construct an adsorbent composite of MgAl-LDH/$LaFeO_3$ utilizing the high phosphate affinity of $LaFeO_3$ and the high anionic exchange capacity of LDHs, aiming for superior removal efficiency of phosphate ions (P-ions). Specifically, the study aims to: (1) prepare the composite through a co-precipitation approach and investigate its phosphate removal efficiency; (2) examine various factors influencing the adsorption process, including pH, temperature, and exposure time; (3) study the adsorption kinetics, isotherms, and thermodynamics to understand the underlying mechanisms; and (4) investigate the reuse capacity of the composite to assess its economic value.

2. Experimental

2.1. Materials

Ferric nitrate nonahydrate [$Fe(NO_3)_3 \cdot 9H_2O$, >99.5%] was obtained from Merck Millipore. Aluminum nitrate nonahydrate [$Al(NO_3)_3 \cdot 9H_2O$, 99.3%], magnesium nitrate hexahydrate [$Mg(NO_3)_2 \cdot 6H_2O$, 98.7%] and lanthanum nitrate nonahydrate [$La(NO_3)_3 \cdot 9H_2O$, 99.8%] were purchased from Sigma-Aldrich. Potassium dihydrogen phosphate [KH_2PO_4, >99%], citric acid [$C_6H_8O_7$, 97%], sodium hydroxide (NaOH, AR) and sodium nitrate (Na_2CO_3, AR) were obtained from Alfa Chemicals.

2.2. Synthesis lanthanum ferrite ($LaFeO_3$)

Synthesis of $LaFeO_3$ was achieved through a sol–gel formation, followed by a calcination step. Initially, 5 mmol of each lanthanum salt and ferric salt (2.1658 g and 2.02 g, respectively) were dissolved in demineralized water (100 mL) at room temperature with continuous stirring for 3 h. Subsequently, citric acid (5 g) was added to the solution and the stirring was continued for another 2 h. The mixture was then heated to 70 °C with continuous stirring to facilitate the evaporation of water to half of its initial volume. The resulting gel was heated in an oven

at 200 °C for 12 h, producing an intermediate fluffy powder exhibiting a highly porous, low-density morphology, arising from the evolution of gaseous byproducts (NO_x, CO_2, H_2O) during the thermal decomposition of citric acid and metal nitrates. The obtained powder was then finely ground and subsequently calcined at 500 °C for 2 h to induce crystallization and formation of the perovskite $LaFeO_3$ phase.[16]

2.3. Preparation of MgAL-LDH/$LaFO_3$

The coprecipitation process was utilized to prepare the MgAl-LDH/$LaFeO_3$ composite. In this process, a solution containing 100 mL of 0.41 M $Mg(NO_3)_2 \cdot 6H_2O$ and 0.21 M $Al(NO_3)_3 \cdot 9H_2O$ was gradually introduced dropwise, at a rate of 2 mL min^{-1}, into a beaker containing 100 mL of 2 M NaOH and 2 M Na_2CO_3 solution. NaOH provides the high pH ($\sim$10) necessary for Mg^{2+} and Al^{3+} hydroxide precipitation and brucite-like layer formation, while Na_2CO_3 supplies carbonate anions (CO_3^{2-}) as the primary interlayer species. These carbonate anions are crucial for stabilizing the positively charged brucite-like layers, as they strongly bind within the interlayer space, preventing collapse of the LDH structure and minimizing incorporation of weaker anions such as –OH or NO_3^- from the metal precursors.[17] Meanwhile, $LaFeO_3$ was incorporated into the mixture at a molar ratio of 0.2 M relative to the total molar concentration, while maintaining the pH of the solution at approximately 10. After completing the precipitation, the obtained gel was aged overnight at room temperature. The gel was then dried overnight at 80 °C, following filtration and thorough washing with distilled water.[18]

2.4. Characterization of adsorbent

The characterization of the prepared adsorbent, MgAl-LDH/$LaFeO_3$, was performed using X-ray diffraction (XRD) (Proto-AXRD Theta–Theta) to examine the crystallinity. Fourier transform-infrared spectroscopy (FTIR) (Perkin-Elmer-Spectrum Two) was used to verify the chemical composition. To analyze the composite morphology, scanning electron microscopy (SEM) (Thermo Scientific) was utilized, while X-ray photoelectron spectroscopy (XPS) (Thermo Scientific; K-Alpha) was utilized to analyze the composite's elemental composition.

2.5. Phosphate removal experiments

To evaluate the factors affecting P-ion adsorption by the MgAl-LDH/$LaFeO_3$ composite, a standard stock potassium dihydrogen phosphate (KH_2PO_4) solution (1000 mg L^{-1}) was prepared and stored for any required concentrations. Phosphate was measured in accordance with an APHA Method 4500-P using a Hach DR-6000 UV–VIS spectrophotometer. In this method, phosphate reacts with ammonium molybdate and ammonium metavanadate in an acidic medium to form a yellow molybdovanado phosphoric acid complex. Absorbance was read at 430 nm, and phosphate concentrations were calculated from a calibration curve prepared with KH_2PO_4 standards.

The effects of various parameters were investigated, including the pH of the solution, temperature, MgAl-LDH/$LaFeO_3$ composite dose, time, and initial P-ion concentration.

The pH was examined in the range of 2–11 using 10 mg of the MgAl-LDH/LaFeO$_3$ composite and 20 mL of a 200 mg L^{-1} P-ions solution at 25 °C. The effect of the temperature, as well as the thermodynamic parameters, was studied in the temperature range from 25 to 55 °C using 10 mg of the MgAl-LDH/LaFeO$_3$ composite and 20 mL of a 200 mg L^{-1} P-ion solution at pH 2. The effect of the MgAl-LDH/LaFeO$_3$ composite dose was tested in a 20 mL volume of a 200 mg L^{-1} P-ion solution at pH 2 and 25 °C using different amounts of MgAl-LDH/LaFeO$_3$ (10–30 mg). To investigate the impact of the initial concentration and the kinetic and isotherm parameters, 10 mg of MgAl-LDH/LaFeO$_3$ was soaked in 20 mL of P-ions of different initial concentrations (100–500 mg L^{-1}) at 25 °C and pH 2. The P-ions removal efficacy ($R\%$) was calculated using eqn (1), while the adsorption capacity (q) was calculated using eqn (2).

$$R\% = \frac{C_0 - C_t}{C_0} \times 100 \qquad (1)$$

$$q = C_0 - C_t \times \frac{V_L}{m_g} \qquad (2)$$

where C_0 and C_t represent the initial and equilibrium concentrations of P-ions in mg L^{-1}, respectively, V represents the solution volume in liters, and m is the MgAl-LDH/LaFeO$_3$ composite dose in grams.

2.6. Selectivity

To assess the selectivity of the MgAl-LDH/LaFeO$_3$ composite for P-ions, competitive adsorption studies were carried out. A certain mass of the MgAl-LDH/LaFeO$_3$ composite (10 mg) was soaked in a beaker containing P-ions (10 mL, 100 mg L^{-1}), along with a solution (10 mL, 100 mg L^{-1}) of a competing anion (nitrate NO$_3^-$, bicarbonate HCO$_3^-$, chloride Cl$^-$, and sulfate SO$_4^{2-}$).

3. Results and discussion

3.1. MgAl-LDH/LaFeO$_3$ characterization

3.1.1 XRD analysis. The XRD patterns for pristine LaFeO$_3$ and MgAl-LDH, as well as the final composite MgAl-LDH/LaFeO$_3$, are presented in (Fig. 1a). For pristine LaFeO$_3$, peaks at $2\theta = 22.6°, 32.3°, 39.7°, 46.1°, 57.5°,$ and $67.4°$ corresponding to the planes (002, 200, 113, 004, 312, and 041, respectively) confirm the crystalline LaFeO$_3$ phase with orthorhombic assembly.[19,20] For MgAl-LDH, a typical crystalline pattern was observed, exhibiting narrow, high-intensity reflections at $2\theta = 11.4°, 23.1°, 34.6°, 38.6°, 46°, 60.5°$ and $62.1°$ for the planes (003), (006), (012), (115), (118), (110) and (113), respectively.[21,22] For the composite, there were distinct peaks of both LaFeO$_3$ and MgAl-LDH, confirming the successful fabrication of MgAl-LDH/
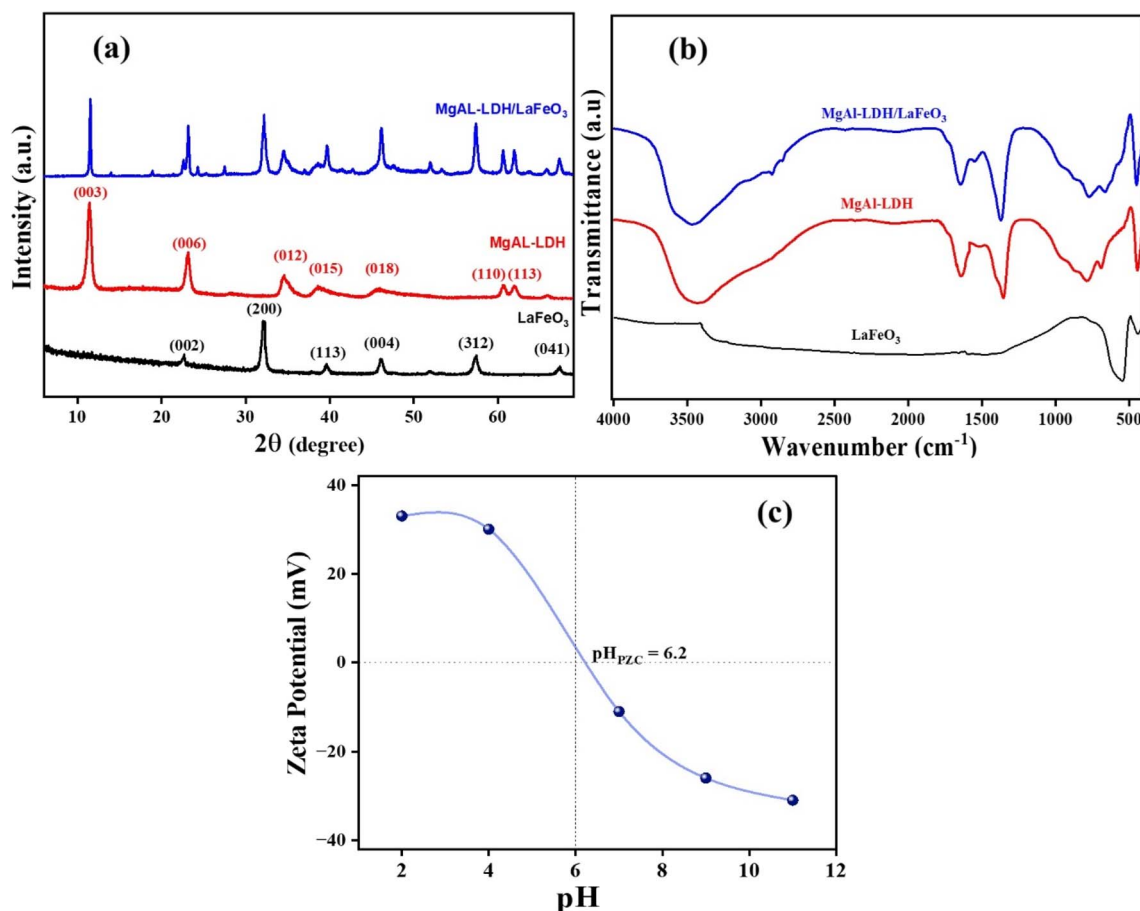

Fig. 1 XRD patterns (a) and FTIR spectra (b) for LaFeO$_3$, MgAl-LDH and the MgAl-LDH/LaFeO$_3$ composite, and the zeta potential at different pH values (c) for the MgAl-LDH/LaFeO$_3$ composite.

LaFeO$_3$. All the characteristic diffraction peaks of both LaFeO$_3$ and MgAl-LDH are present, confirming the coexistence of the two crystalline phases without the formation of any major impurities.[23,24] The strong (003) and (006) low-angle reflections confirm the presence of stacked brucite-like layers, verifying the formation of a well-ordered LDH structure within the composite.[21,25] The LaFeO$_3$ peaks in the composite show no significant shift in position, indicating that its perovskite lattice remains unaltered. However, there is a slight broadening and reduction in intensity. This indicates that MgAl-LDH is dispersed onto or intergrown with LaFeO$_3$, resulting in a slight decrease in the LaFeO$_3$ crystallite size or minor interfacial distortions.[26] Similarly, the LDH reflections exhibit lower relative intensity than pure LDH, which can be attributed to smaller LDH crystallite domains and partial coverage by the highly crystalline LaFeO$_3$ phase.[27]

3.1.2 FTIR.

FTIR spectra of pristine LaFeO$_3$, MgAl-LDH, as well as the final composite MgAl-LDH/LaFeO$_3$ are presented in Fig. 1b. For neat LaFeO$_3$, the sharp peak at 547 cm^{-1} is attributed to the Fe–O stretching vibration, being characteristics for LaFeO$_3$.[28] MgAl-LDH shows a typical LDH spectrum with a wide peak at 3433 cm^{-1} attributed to O–H stretching. Another sharp peak at 1633 cm^{-1} was observed, corresponding to the interlayer H$_2$O bending vibration.[29,30] The broad band observed at ~1385 cm^{-1}, together with the out-of-plane bending mode in the ~850–870 cm^{-1} region, can be attributed primarily to the presence of interlayer carbonate (CO$_3^{2-}$).[31] However, nitrate salts were used as metal precursors during LDH synthesis. Since nitrate (NO$_3^-$) anions exhibit vibrational absorptions in a similar band region, it is reasonable to assume that traces of NO$_3^-$ may coexist with CO$_3^{2-}$ in the interlayer space.[32] The spectral overlap of nitrate with carbonate could therefore contribute to the single, intense band observed near 1385 cm^{-1}.[31] Nevertheless, carbonate possesses a significantly higher affinity for LDH interlayers compared to nitrate, due to their higher charge density and stronger electrostatic binding affinity toward the positively charged brucite-like layers.[33] The broad band observed in the 400–800 cm^{-1} region, and particularly the features below 500 cm^{-1}, can be attributed to the overlapping stretching and bending vibrations of metal–oxygen bonds within the composite structure (M–O, where M = Mg, Al, Fe, and La).[34] This includes Fe–O stretching vibrations from the LaFeO$_3$ perovskite phase, typically found between 400–600 cm^{-1}, while La–O vibrations in lanthanum ferrite/perovskite lattices also contribute within the same region, often overlapping with Fe–O modes and thus giving rise to broadened spectral features in the 400–600 cm^{-1} range.[35] In addition, the band near 430–460 cm^{-1} can be more explicitly assigned to Mg–O stretching vibrations arising from the brucite-like layers of MgAl-LDH.[36] For the MgAl-LDH/LaFeO$_3$ composite, all the characteristic peaks of LaFeO$_3$ and MgAl-LDH are shown, reflecting the successful preparation of the LDH/LaFeO$_3$ composite.

3.1.3 MgAl-LDH/LaFeO$_3$ surface charge.

The zeta potential (ZP) measurement reveals the effect of the medium pH on the surface charge of the MgAl-LDH/LaFeO$_3$ composite, and hence affects the electrostatic attraction between the LDH/LaFeO$_3$ composite and P-ions. As presented in Fig. 1c, the LDH/LaFeO$_3$ composite has a positive zeta potential as high as +32.1 mV at pH 2 and a point of zero charge (pH$_{PZC}$) equal to 6.2. The highly positive zeta potential at pH 2 originates primarily from the protonation of surface hydroxyl groups (M–OH, where M = Mg, Al, Fe, or La) under strongly acidic conditions. The governing equilibrium can be expressed as: (M–OH + H$^+$ $\rightleftharpoons$ M–OH$_2^+$). At pH 2, the high proton activity shifts this equilibrium strongly toward the right, leading to the extensive formation of (M–OH$_2^+$) species. This surface protonation is consistent with classical acid–base surface chemistry and explains the net positive charge of the composite.[37] This high positively charged surface suggests the possibility of high electrostatic attraction of P-ions with the LDH/LaFeO$_3$ composite, enhancing their adsorption onto the surface. In contrast, at higher pH values beyond 6.2, the ZP values decreased to −25.3 mV at pH 9 and −31 at pH 11. As the surface charge transitioned from positive to increasingly negative, the electrostatic attraction diminished. This variation in surface charge highlights the crucial role of pH in governing the adsorption efficiency of the material.

3.1.4 Morphology.

SEM was utilized to investigate the morphology of the pristine materials, as well as the MgAl-LDH/LaFeO$_3$ composite. As shown in Fig. 2a and b, SEM images of LaFeO$_3$ reveal the formation of spherical particles that exhibit some level of agglomeration. A limited number of larger, loosely aggregated clusters were observed, likely resulting from aggregation processes that occur during the washing stages, as well as the elevated temperatures used during the calcination process. The SEM images of MgAl-LDH (Fig. 2c and d) predominantly feature well-defined hexagonal platelet structures, which exhibit minor cracks along the edges of the hexagonal sheets, with some sheets displaying vertical intersections at their hexagonal sides. These vertical crossings may result from the sharing of aluminum hydroxide seeds during the crystal formation phase, leading to perpendicular intersections that minimize surface energy by reducing exposed areas. Additionally, the presence of small defects along the hexagonal edges may indicate incomplete crystallization.[6] The SEM of the MgAl-LDH/LaFeO$_3$ composite (Fig. 2e and f) clarified the coating of the spherical LaFeO$_3$ particles on hexagonal MgAl-LDH.

3.1.5 XPS analysis.

The XPS analysis of the MgAl-LDH/LaFeO$_3$ composite (Fig. 3a) clarified the existence of Mg, Al, La, Fe, and O elements, confirming the successful formation of the LaFeO$_3$ modified MgAl/LDH composite.[23] The Mg 1s and spectrum (Fig. 3b) revealed the presence of metal oxides and hydroxides, with two peaks at 1304.35 eV and 1306.1 eV, which are characteristic for Mg^{2+} in a hydroxide/oxide medium. The spectrum for Al 2p (Fig. 3c) revealed the existence of an Al 2p$_{1/2}$ characteristic peak at 74.47 eV that is attributed to Al^{3+} cations in an octahedral coordination environment, corresponding to Al–O bonds within the brucite-like LDH layers.[38] The La 3d spectrum (Fig. 3d) showed characteristic peaks for La^{3+} at 854.55 eV (La 3d$_{3/2}$) and 837.86 eV (La 3d$_{5/2}$).[39] The Fe 2p spectrum (Fig. 3e) exhibited binding energies for Fe 2p$_{3/2}$ at 713.98 eV and Fe 2p$_{1/2}$ at 728.33 eV, along with a satellite peak at 720.88 eV, indicating the presence of Fe^{3+} which is consistent
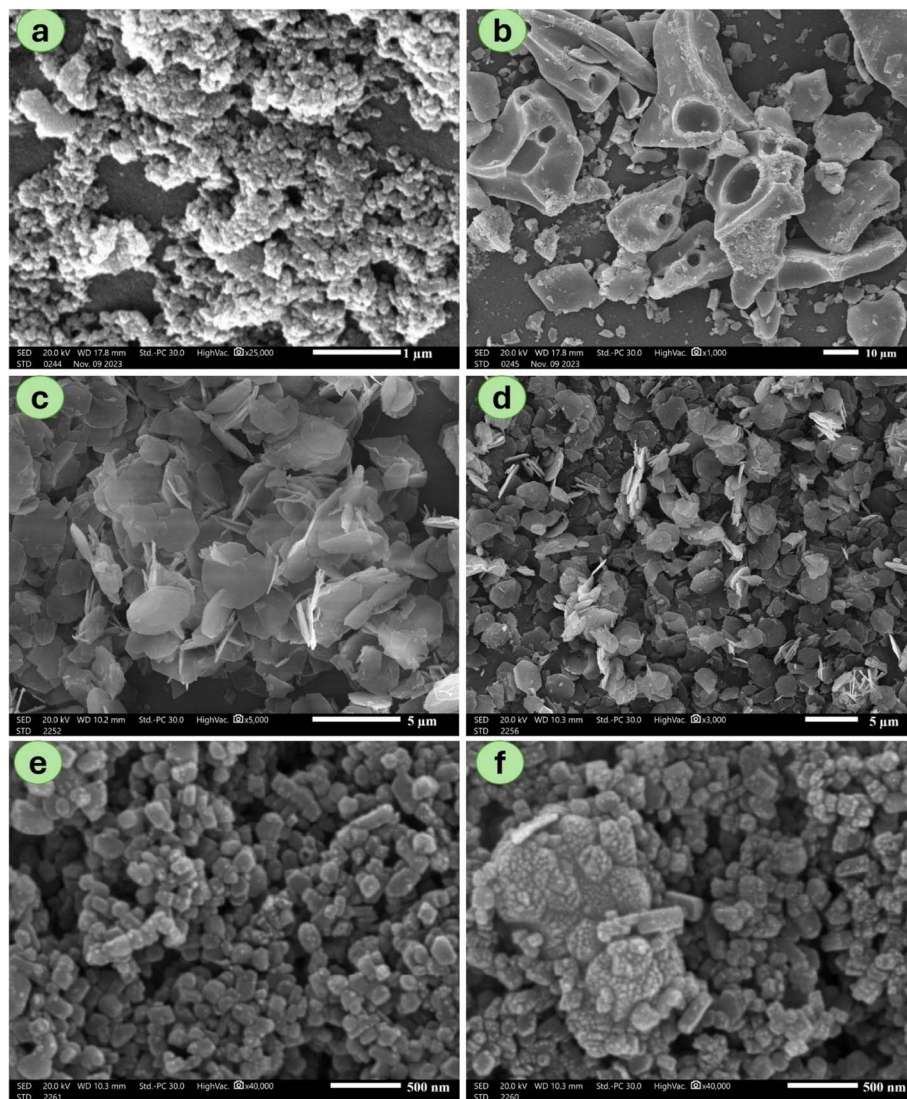
Fig. 2   SEM images of LaFeO$_3$ (a and b), MgAl-LDH and (c and d) and the MgAl-LDH/LaFeO$_3$ composite (e and f).

with LaFeO$_3$.[26] The smaller doublet with Fe 2p$_{3/2}$ at 709.8 eV suggests the presence of a small fraction of Fe^{2+}, which may result from surface reduction or synthesis-induced defects. Additionally, the O 1s spectrum (Fig. 3f) displayed peaks corresponding to lattice oxygen in metal–oxygen bonds (M–O, where M = Mg, Al, La, and Fe), at 531.72 eV and surface hydroxyl groups (M–OH) at 532.45 eV, indicating the presence of the oxygen species in the structure.[38]

3.2. Adsorption performance of the MgAl-LDH/LaFeO$_3$ composite

3.2.1 Comparison test. Fig. 4a illustrates the comparative adsorption performance of pristine LaFeO$_3$, MgAl-LDH (1 : 1), and MgAl-LDH (2 : 1) toward phosphate ions. The corresponding adsorption capacities were determined to be 218 mg g^{-1}, 210 mg g^{-1} and 302 mg g^{-1}, with removal efficiencies of 55.9%, 58.9%, and 77.5%, respectively. As a result, the 2 : 1 ratio was selected for the fabrication of the composite. The adsorption

capacities for MgAl-LDH to LaFeO$_3$ with ratios of 0.1, 0.2 and 0.3 M of LaFeO$_3$ were found to be 302 mg g^{-1}, 372 mg g^{-1}, and 374 mg g^{-1}, respectively, and the removal efficiencies were 90%, 95.4%, and 95.8%. Based on these findings, the MgAl-LDH 2 : 1/ LaFeO$_3$ (0.2 M) was identified as the optimal formulation. Interestingly, the increase of the LaFeO$_3$ ratio to 0.3 M did not yield a significant improvement in the adsorption performance. This could be a result of the plateau effect, where the additional LaFeO$_3$ likely led to particle aggregation and pore blocking, rather than the creation of new accessible active sites.[24,40] Consequently, a LaFeO$_3$-to-total metals (Mg^{2+} + Al^{3+}) ratio of 0.2 M was identified as optimal for this study. This selection was also justified for economic considerations as lanthanum is costlier than magnesium or aluminum. Therefore, minimizing the LaFeO$_3$ content while maximizing the adsorption efficacy is a crucial factor for the large-scale application and economic viability of the composite adsorbent.[41]

3.2.2 Effect of pH. The solution pH effect on P-ion adsorption by the MgAl-LDH/LaFeO$_3$ composite was examined
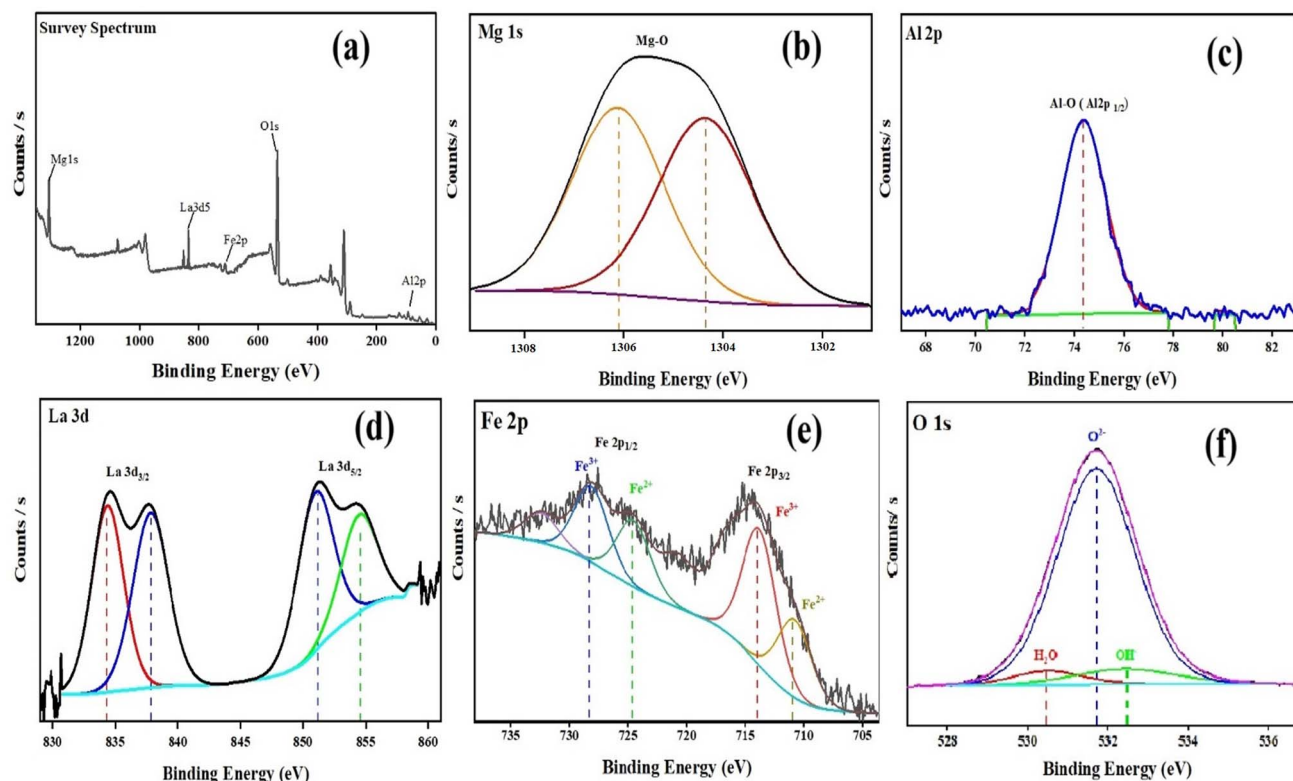
Fig. 3 XPS spectra of the MgAl–LDH/LaFeO$_3$ composite: (a) survey-spectrum and (b) Mg 1s, (c) Al 2p, (d) La 3d, (e) Fe 2p, and (f) O 1s spectra.

across a wide pH range (2–9). The results (Fig. 4b) demonstrated that a superior adsorption capacity of 372 mg g^{-1} and removal efficiency of 96% were achieved at pH 2. Upon increasing pH, the adsorption capacity gradually declined at pH 4 and 7, with a significant drop at pH 9 and reached an adsorption capacity as low as 44 mg g^{-1} at pH 11.[42] This behavior is attributed to the dominant phosphate species present at different pH levels: $H_2PO_4^-$ is predominant between pH 2.15 and 7.20, while HPO_4^{2-} becomes the dominant species from pH 7.20 to 10.0. Since $H_2PO_4^-$ has a lower adsorption-free energy, it is more readily adsorbed onto the MgAl–LDH/LaFeO$_3$ composite surface.[43] At low pH, the surface of the composite is protonated and positively charged. This was confirmed by zeta potential measurements of +32.1 mV at pH 2 and +30.4 mV at pH 4, which enhanced the electrostatic attraction between the MgAl–LDH/LaFeO$_3$ composite surface and negatively charged phosphate ions.[44] Furthermore, La and Fe contribute to phosphate removal through direct interactions because of their ability to form Lewis acidic sites, binding phosphate anions *via* coordination bonds or ligand exchange. Conversely, the MgAl–LDH/LaFeO$_3$ composite became negatively charged at higher pHs, with zeta potential values of −11.2 mV at pH = 6 and −25.3 mV at pH = 9, which hinder the attraction between the negatively charged MgAl–LDH/LaFeO$_3$ composite surface and the negatively charged P-ions.[45]

3.2.3 Effect of the initial P-ion concentrations. To assess how the initial concentration of P-ions affect the performance of the MgAl–LDH/LaFeO$_3$ composite, different initial P-ion concentrations were utilized (100–500 mg L^{-1}), as presented in Fig. 4c. The results revealed that the adsorption capacity increased from 200 to 802 mg-P per g as the P-ion concentration increased from 200 to 500 mg L^{-1}. This could be explained by the fact that at higher concentrations, both available P-ions as well as the diffusion rate of P-ions increased at elevated concentrations. This increase in the diffusion rate accelerates the transfer of P-ions from the bulk solution to the surface of the MgAl–LDH/LaFeO$_3$ composite. Consequently, more P-ions are adsorbed, leading to a higher adsorption capacity value.[46]

3.2.4 Effect of composite dosage. The effect of the MgAl–LDH/LaFeO$_3$ composite dosage on the P-ion removal (Fig. 4d) revealed that 10 mg of MgAl–LDH/LaFeO$_3$ achieved 95.4% removal with a capacity of 372 mg-P per g, while 30 mg of MgAl–LDH/LaFeO$_3$ achieved 99.7% removal efficacy with a capacity of 129 mg-P per g. The slight increase in the removal percentage is due to the availability of more surface sites for adsorption as more MgAl–LDH/LaFeO$_3$ composite is added. However, the decrease in adsorption capacity occurs because, all types of adsorption sites, including high-energy sites, are fully accessible to phosphate ions at lower dosages, leading to rapid saturation. As the dosage increases, fewer high-energy sites are available and more low-energy sites are occupied, which reduces the overall adsorption capacity. This behavior reflects the heterogeneity of the LDH surface, where adsorption sites have varying binding energies, highlighting the balance between the removal efficiency and adsorption capacity when adjusting the adsorbent dosage.[47,48]
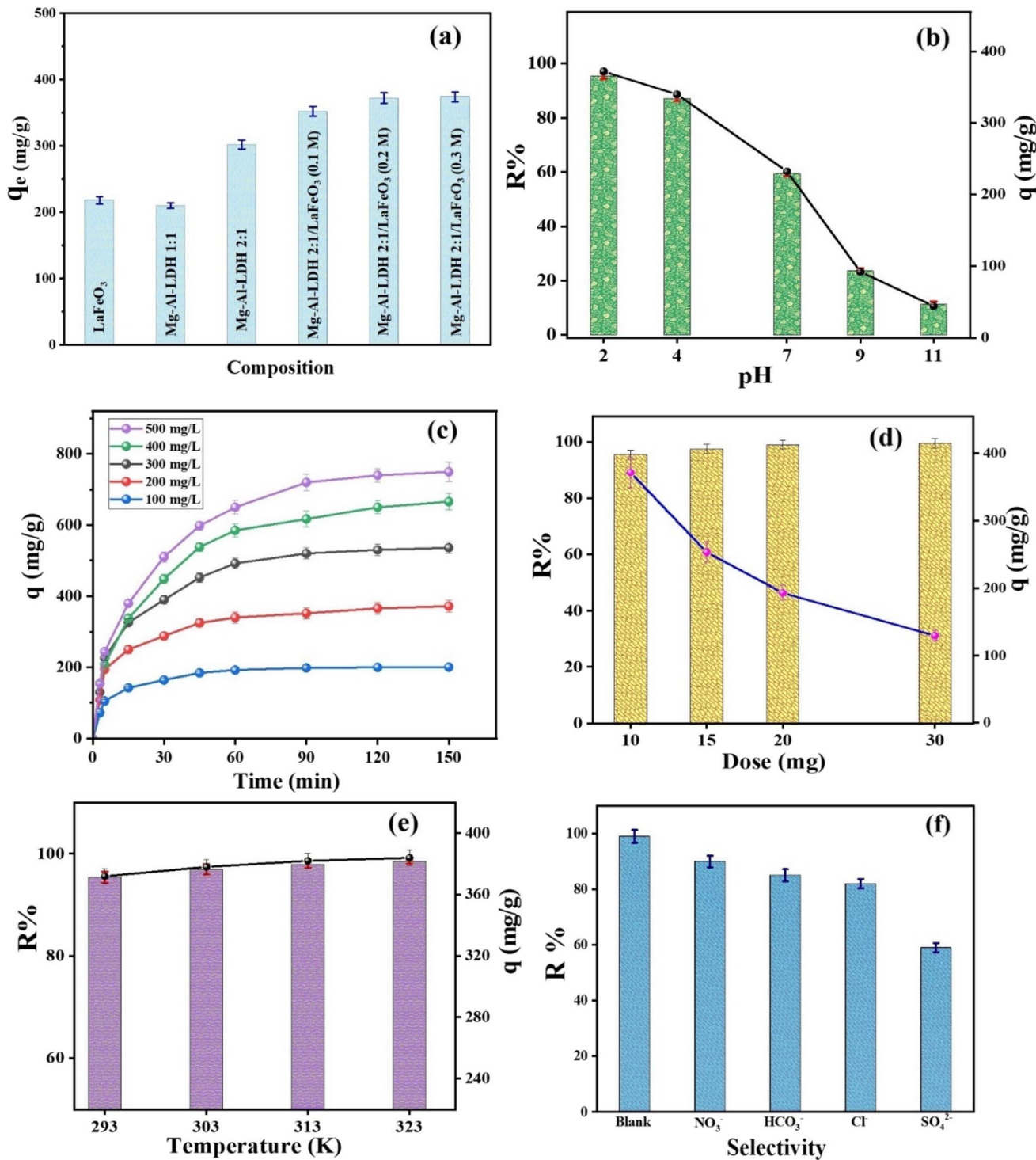
Fig. 4 Optimization of phosphate adsorption on the MgAl-LDH/LaFeO$_3$ composite: (a) composite composition, (b) pH, (c) initial P-ion concentration, (d) dose, (e) temperature, and (f) selectivity.

3.2.5 Effect of temperature. The temperature has a great effect on the adsorption efficiency and capacity. On this basis, the removal of P-ions by the MgAl-LDH/LaFeO$_3$ composite was examined at different temperatures, as shown in Fig. 4e. The removal efficiency and the capacity increased from 372 to 384 mg g^{-1} with increasing temperature from 25 to 50 °C,

reflecting the endothermic nature of the process. This indicates that higher temperatures provide additional energy, enhancing the mobility of phosphate ions in the solution and promoting stronger interactions with the active sites of the MgAl-LDH/LaFeO$_3$ composite. This reflects the activating and facilitating rule of heat in the removal process.[49]
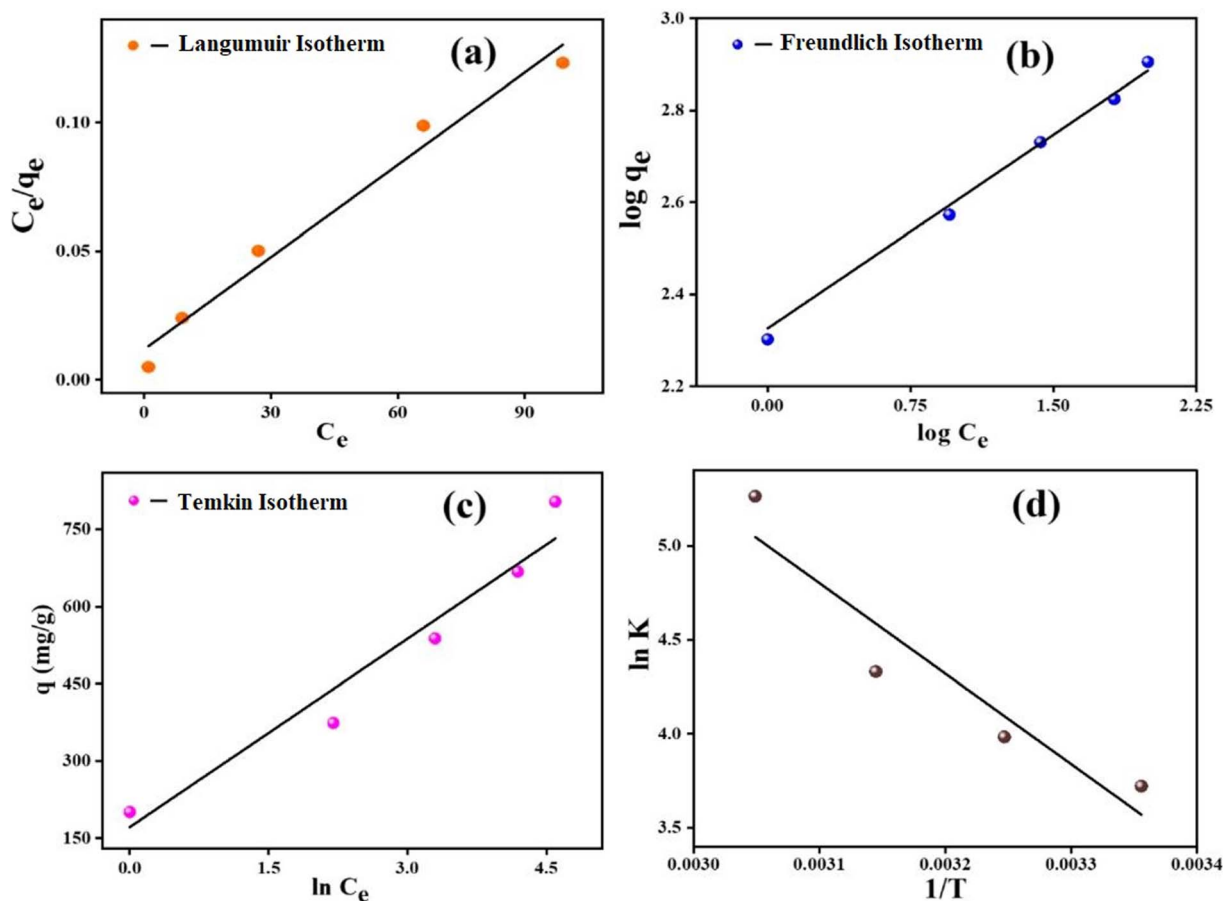
Fig. 5 Adsorption isotherms of the MgAl-LDH/LaFeO$_3$ composite: (a) Langmuir, (b) Freundlich, and (c) Temkin models. (d) Adsorption thermodynamics.

3.2.6 Selectivity. Indeed, real wastewater contains many anions, such as NO_3^-, SO_4^{2-}, Cl^- and HCO_3^-, that can compete with P-ions for the adsorption on MgAl-LDH/LaFeO$_3$. These anions could challenge the adsorption of P-ions in the interlayer spaces of LDHs that have a large surface area, high anion exchange capacity, and adaptable interlayer space that accommodates a variety of anionic pollutants. Based on this fact, the removal efficiency of P-ions by MgAl-LDH/LaFeO$_3$ was examined in the presence of these ions (Fig. 4f). Results indicated that the removal efficiency of P-ions by MgAl-LDH/LaFeO$_3$ in the presence of competing anions was in the following order: NO_3^- > HCO_3^- > Cl^- > SO_4^{2-}. The adsorption capacity experienced a slight reduction in the presence of nitrate and bicarbonate, while sulfate caused a significant decrease in phosphate removal. This aligns with previous research demonstrating that LDHs exhibit higher affinity for divalent anions like sulfate

compared to monovalent anions. These findings highlight the competitive effects of common anions in wastewater and the selective adsorption behavior of the composite.[50,51]

3.3. Adsorption isotherm

P-ions adsorption on the MgAl-LDH/LaFeO$_3$ composite was evaluated using different isotherm models, including Freundlich, Langmuir, and Temkin. Eqn (3)–(5) represent the linear forms of these isotherms:

Langmuir

$$\frac{C_e}{q_e} = \frac{1}{b\,q_m} + \frac{C_e}{q_m} \qquad (3)$$

Freundlich

Table 1 Adsorption isotherm parameters derived from different models for the adsorption of P-ions by the MgAl-LDH/LaFeO$_3$ composite

Isotherm	Langmuir			Freundlich			Temkin		
Parameter, unit	q_{max}, mg g^{-1}	b, L mg^{-1}	R^2	k_f, L mg^{-1}	n	R^2	B_1, J mol^{-1}	B, kJ mol^{-1}	R^2
	833.3	0.11	0.969	10.23	3.55	0.993	18.57	0.133	0.919

Table 2 Thermodynamic parameters of P-ion removal by the MgAl-LDH/LaFeO$_3$ composite

Temperature (K)	ΔG° (kJ mol^{-1})	ΔH° (kJ mol^{-1})	ΔS° (J mol^{-1} K^{-1})
298	−9.22	40.02	163.95
308	−10.20		
318	−11.45		
328	−14.35		

$$\log q_\mathrm{e} = \log k_\mathrm{f} + \frac{1}{n} \log C_\mathrm{e} \qquad (4)$$

Temkin

$$q_\mathrm{e} = B_1 \log A + B_1 \log C_\mathrm{e} \qquad (5)$$

here, q_e and q_m represent the adsorption capacity at equilibrium and the maximum adsorption capacity (mg g^{-1}), respectively, C_e symbolizes the concentration at equilibrium (mg L^{-1}), b represents the Langmuir constant, k_f and n represent Freundlich constants, B_1 represents the Temkin constant, and A represents the equilibrium bond constant.

From the results of the linear plots (Fig. 5a–c) and (Table 1), the adsorption process was best described by the Freundlich model, with the highest correlation coefficient ($R^2 = 0.993$).

These findings suggest that the process is influenced more with physical adsorption mechanisms occurring on a surface with a non-uniform energy distribution, which supports the formation of multilayer adsorption.[52] The Langmuir model revealed that the q_max is 833.3 mg-P per g. The results obtained from the Temkin model revealed that the physisorption process is favorable since the obtained b value is <80 kJ mol^{-1}.[53]

3.4. Adsorption thermodynamics

The temperature effect (298 to 313 K) on P-ion removal by the MgAl-LDH/LaFeO$_3$ composite was examined (Fig. 5d). These parameters were computed using eqn (5) and (6).[54] Table 2 summarizes the thermodynamic parameters, standard change in enthalpy (ΔH°), standard change in entropy (ΔS°), and standard change in the Gibbs free energy (ΔG°).

$$\ln K_\mathrm{e} = \frac{\Delta S^\circ}{R} - \frac{\Delta H^\circ}{RT} \qquad (6)$$

$$\Delta G^\circ = -RT \ln k_\mathrm{e} \qquad (7)$$

where, the equilibrium constant is K_e and the universal gas constant $R = 8.314$ J mol^{-1} K^{-1}, and the Kelvin temperature is T.

The results revealed that ΔG° has negative values, confirming the feasibility of the adsorption of P-ions by the MgAl-LDH/LaFeO$_3$ composite. Furthermore, the negative value of ΔG°
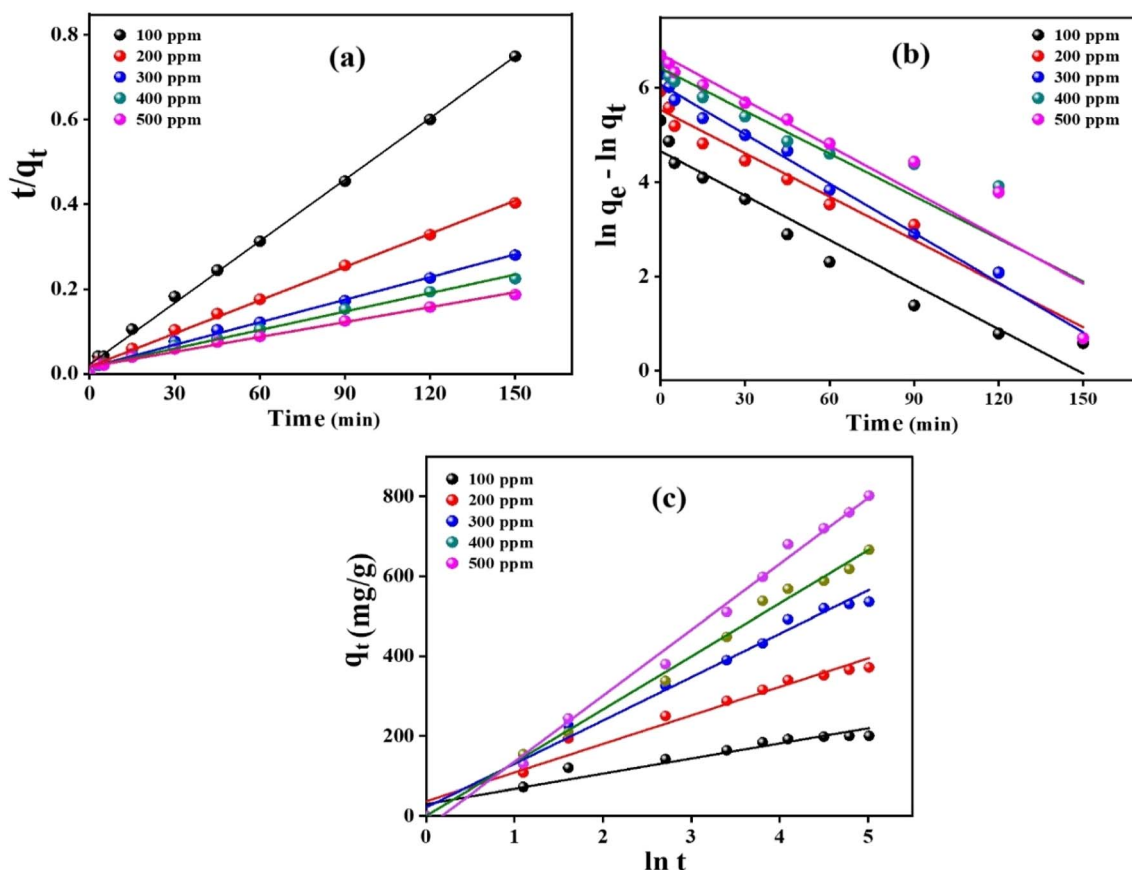

Fig. 6 Kinetic study of adsorption: (a) pseudo-1st-order, (b) pseudo-2nd-order, and (c) Elovich models.

Table 3 Kinetic parameters of adsorption of P-ions by MgAl-LDH/LaFeO₃

Parameters	Concentration (mg L^{-1})				
	100	200	300	400	500
$q_{e,exp}$ (mg g^{-1})	200.2	372	536	666	802
Pseudo-1st-order					
k_1 (min^{-1})	0.031	0.030	0.035	0.033	0.032
$q_{e,cal}$ (mg g^{-1})	105.6	254.6	432.6	610.9	820.6
R^2	0.935	0.975	0.992	0.859	0.892
Pseudo-2nd-order					
K_2 (min^{-1})	0.00321	0.00035	0.00037	0.00041	0.00043
$q_{e,cal}$ (mg g^{-1})	206.3	382.8	561.3	684.9	854.7
R^2	0.998	0.997	0.993	0.990	0.986
Elovich					
α (mg g^{-1})	82.93	119.56	132.09	133.14	138.1
β (mg g^{-1})	0.026	0.014	0.009	0.007	0.006
R^2	0.929	0.963	0.988	0.994	0.993

increased with the temperature increase, reflecting the feasibility of the process with increasing temperature. However, the positive $\Delta H°$ value reveals that the process is endothermic in nature.[55] The positive $\Delta S°$ value reveals the diffusion of P-ions at the MgAl-LDH/LaFeO₃ composite–liquid interface.

3.5. Kinetic studies

To evaluate the kinetics of phosphate adsorption on the MgAl-LDH/LaFeO₃ composite, adsorption experiments were carried out at different initial concentrations of P-ions (100–500 mg L^{-1}).

The kinetic data were examined using pseudo-1st-order, pseudo-2nd-order, and Elovich models (Fig. 6a–c). Table 3 summarizes the main kinetic parameters obtained from the linear plots of these models. The obtained parameters clarified that the pseudo-2nd-order model provided the best fit for the experimental data, with higher R^2 values compared to the pseudo-1st-order model. Additionally, $q_{e,cal}$ values from the
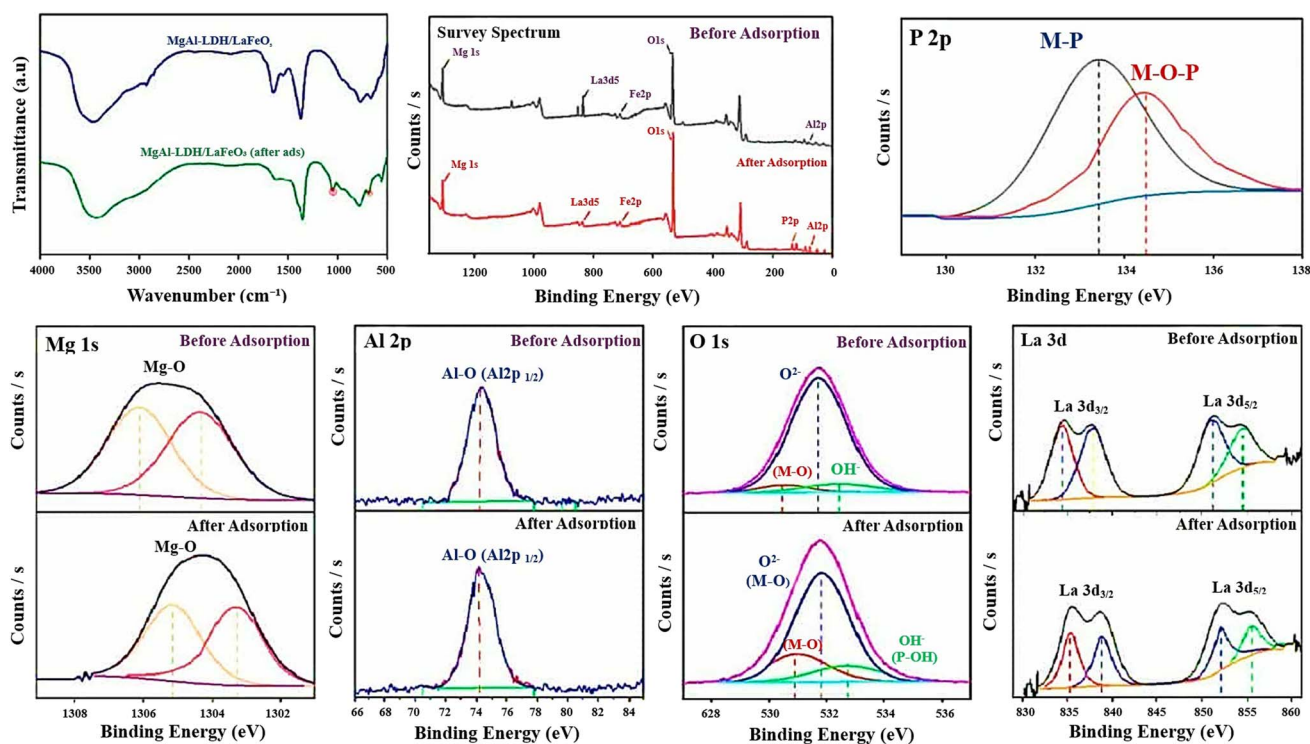

Fig. 7 Characterization of the used MgAl-LDH/LaFeO₃ composite. (a) FTIR, (b) XPS survey, (c) P 2p spectra, (d) Mg 1s spectra, (e) Al 2p spectra, (f) O 1s spectra, and (g) La 3d spectra.

pseudo-second-order model closely matched the experimental ones, confirming the model's accuracy.[56] The Elovich model also showed relatively high R^2 values (>0.929), supporting the involvement of both chemisorption and surface adsorption. These findings collectively demonstrate that the adsorption process for P-ions on MgAl-LDH/LaFeO$_3$ is primarily controlled by chemisorption, with some contribution from surface interactions.[57]

3.6. Mechanism of P-ions adsorption by MgAl-LDH/LaFeO$_3$

P-ion adsorption by the MgAl-LDH/LaFeO$_3$ composite was confirmed through FTIR (Fig. 7a) and XPS (Fig. 7b) analyses post-adsorption. The FTIR spectrum revealed the emergence of a new peak at 1054 cm^{-1}, confirming the P-ion adsorption onto the MgAl-LDH/LaFeO$_3$ composite surface.[58] Additionally, the wide-scan XPS spectrum of MgAl-LDH/LaFeO$_3$ after adsorption exhibited a characteristic P 2p peak, further validating the adsorption process. The high-resolution P 2p spectrum (Fig. 7c) displayed two distinct peaks between 133.43 and 134.5 eV, attributed to P 2p$_{3/2}$ and P 2p$_{1/2}$,[39] respectively, confirming the successful incorporation of P-ions into the composite structure. The adsorption of P-ions onto MgAl-LDH/LaFeO$_3$ occurs through a combination of electrostatic attraction, ligand exchange, complexation, surface precipitation, and ion exchange, as supported by FTIR and XPS analyses. These mechanisms are detailed below.

3.6.1 Electrostatic attraction. At low pH levels, the MgAl-LDH/LaFeO$_3$ composite exhibits a high positive surface charge, as confirmed by zeta potential measurements, leading to strong electrostatic interactions with negatively charged P-ions. This attraction facilitates the initial adsorption of P-ions onto the MgAl-LDH/LaFeO$_3$ surface. However, as the pH increases,

competition with hydroxide ions (OH$^-$) retards the phosphate adsorption efficiency due to charge repulsion effects.[59]

3.6.2 Ligand exchange. Ligand exchange involves surface coordination, where phosphate directly binds to metal–OH groups *via* inner-sphere complexation, without displacing the interlayer anions. The FTIR spectra after P-ion adsorption revealed the formation of M–O–P bonds, indicating that P-ions bind to metal hydroxyl (–OH) groups *via* ligand exchange (eqn (8)). The appearance of a new peak at 1054 cm^{-1},[58] attributed to P–O complexation, further confirms this interaction. Additionally, there is a shift in the stretching vibration of O–H from 3457 to 3447 cm^{-1} that supports ligand exchange, as hydroxyl (–OH) groups are substituted by phosphate anions.[60]

$$MOH + H_2PO_4^- \rightarrow MH_2PO_4 + OH^- \tag{8}$$

3.6.3 Complexation. A new peak at 1051 cm^{-1} was observed after P-ion adsorption (Fig. 7a), attributed to phosphate complexation with hydroxyl groups on the MgAl-LDH/LaFeO$_3$ composite. Furthermore, the shift in La 3d$_{5/2}$ and La 3d$_{3/2}$ binding energies (Fig. 7d) to lower values suggests electronic perturbation within the La 4f valence orbital. This indicates inner-sphere coordination complex formation between lanthanum and phosphate ions, leading to La–O–P bond formation. These findings highlight lanthanum's strong affinity for phosphate ions, reinforcing its critical role in the adsorption process.[23] Furthermore, the O 1s spectrum (Fig. 7f) shows variations in the M–O and M–OH binding energies, further supporting the substitution of hydroxyl (–OH) groups by phosphate, resulting in the formation of M–P bonds.[27]

3.6.4 Ion exchange. XPS analysis provides further evidence of ion exchange, confirming the substitution of P-ions at metal
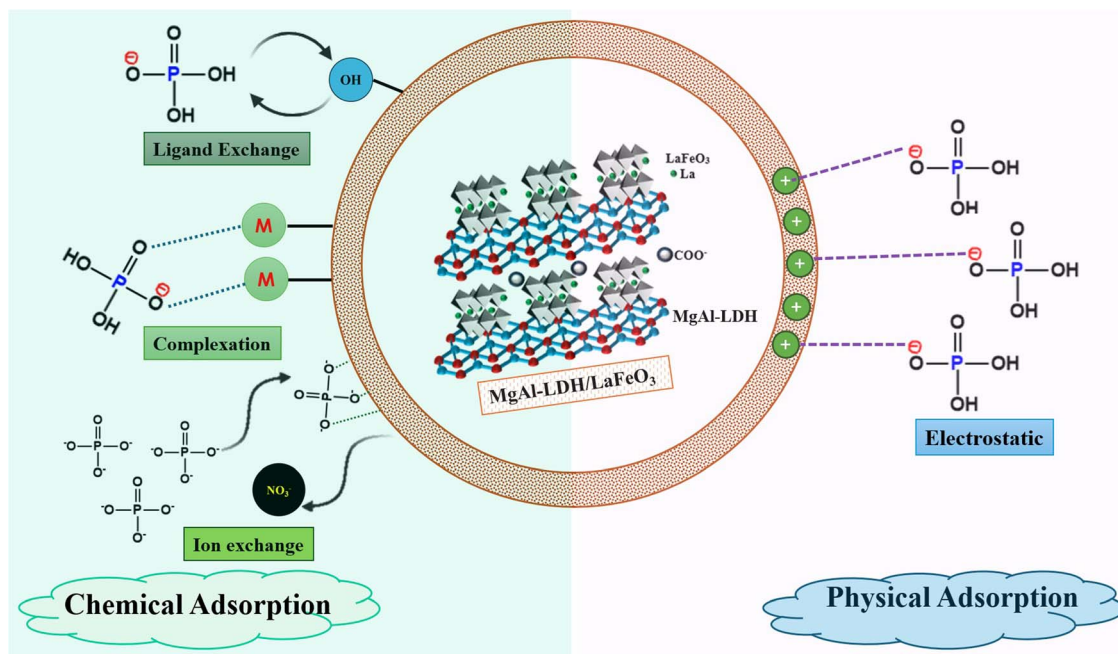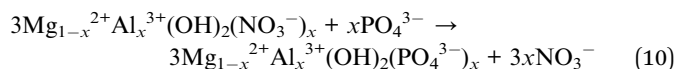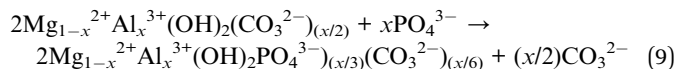

Fig. 8 Adsorption mechanism of P-ions by the MgAl-LDH/LaFeO$_3$ composite.

Table 4 Comparison of the maximum adsorption capacity of the MgAl-LDH/LaFeO$_3$ composite with other pertinent adsorbents for phosphate removal

Adsorbent	pH	Dosage (g L^{-1})	Q (mg P per g)	Ref.
MgAl LDH nanoparticles using urea as a dispersing agent	8.5	1.0	300	61
4 : 1 Mg/Al-LDHs biochar	3	2.5	82	62
Zn–Al-LDH	7	—	348	10
Magnetic Fe$_3$O$_4$@MgAl-LDH@La(OH)$_3$	7	0.1	200	63
AC/MgAl LDH composite	6.5	1.0	337	64
Mg/Al LDH	3	0.6	214	18
BBAC@Zn–Al LDH	—	2.0	87	65
CuAl/CF-LDH	8	0.2	100	66
MgAl-LDH/LaFeO$_3$	2	0.5	372	This study

sites. Shifts in Mg 1s (Fig. 7d) from 1304.35 eV to 1303.32 eV and in Al 2p (Fig. 7e) from 74.47 eV to 75.44 eV indicate phosphate interactions with MgAl-LDH sites, supporting the ion-exchange mechanism as a key pathway in phosphate adsorption.[38] An ion-exchange mechanism involving the displacement of interlayer anions such as carbonate ($CO_3{}^{2-}$) and residual nitrate ($NO_3{}^-$) by phosphate species is present in the aqueous phase. Due to the higher charge density and stronger affinity of phosphate ($PO_4{}^{3-}$), it readily replaces the weaker electrostatically bound anions in the LDH interlayers, as illustrated in eqn (9) and (10):

$$2Mg_{1-x}{}^{2+}Al_x{}^{3+}(OH)_2(CO_3{}^{2-})_{(x/2)} \rightarrow \\ 2Mg_{1-x}{}^{2+}Al_x{}^{3+}(OH)_2PO_4{}^{3-}{}_{(x/3)}(CO_3{}^{2-})_{(x/6)} + (x/2)CO_3{}^{2-} \quad (9)$$

$$3Mg_{1-x}{}^{2+}Al_x{}^{3+}(OH)_2(NO_3{}^-)_x + xPO_4{}^{3-} \rightarrow \\ 3Mg_{1-x}{}^{2+}Al_x{}^{3+}(OH)_2(PO_4{}^{3-})_x + 3xNO_3{}^- \quad (10)$$

In summary, the combined evidence from FTIR and XPS analyses confirms that phosphate adsorption on the MgAl-LDH/LaFeO$_3$ composite occurs *via* multiple mechanisms, including electrostatic attraction, ligand exchange, complexation, and ion exchange (Fig. 8). The strong affinity of lanthanum for phosphate ions, along with the structural adaptability of the LDH framework, makes this composite an effective and reusable adsorbent for phosphate removal in water treatment applications.

3.7. Comparison study

The adsorption performance of the developed MgAl-LDH/LaFeO$_3$ composite was compared to adsorbents previously reported in the literature, as summarized in Table 4. The recorded data reveal that the MgAl-LDH/LaFeO$_3$ composite exhibits superior phosphate uptake with a capacity of 372 mg g^{-1}. This remarkable performance is attributed to a synergistic effect within the MgAl-LDH/LaFeO$_3$ composite, where MgAl-LDH provides high capacity for ion exchange and electrostatic interactions, while the dispersed LaFeO$_3$ nanoparticles contribute highly specific Lewis acid sites (La^{3+} and Fe^{3+}) for strong inner-sphere complexation with phosphate anions.

3.8. Reusability of MgAl-LDH/LaFeO$_3$

Reusability of the adsorbent is a crucial factor that determines its economic feasibility. The reusability of the MgAl-LDH/LaFeO$_3$ composite was evaluated over five consecutive adsorption–desorption cycles to assess its long-term performance in phosphate ion removal. After each cycle, the phosphate-loaded composite was washed with an HCl solution (pH $\approx$ 2) and dried before the next run. The obtained results (Fig. 9) reveal that the removal efficiency of the MgAl-LDH/LaFeO$_3$ composite remains remarkably high, with values exceeding 88% after the fifth cycle. The minimal decline in efficiency and adsorption capacity over successive cycles confirms that the composite retains its structural integrity with no evidence for the leaching of metals ions or dissolution of the adsorbent framework even after multiple regeneration steps. These findings highlight its excellent stability, which can be assigned to the chemical stability of LaFeO$_3$. Perovskites are used in acidic media due to their strong, stable and crystalline structure so that they may shield parts of LDH from direct acid contact. Furthermore, the rapid adsorption of phosphate anions, which can form insoluble metal–phosphate complexes on the surface, potentially passivating the surface and protecting the underlying material from further dissolution. This makes it a promising, stable material for sustainable and cost-effective water treatment applications.
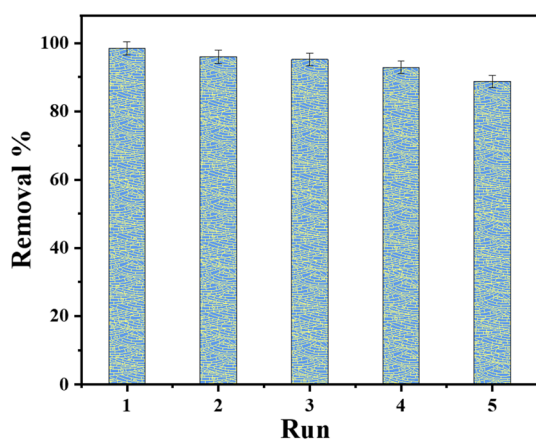
Fig. 9 Reusability of the MgAl-LDH/LaFeO$_3$ composite for the removal of P-ions.

4. Conclusion

The MgAl-LDH/LaFeO₃ composite demonstrates a highly effective solution for phosphate ion removal from aqueous solutions, addressing a critical challenge in water eutrophication. Characterized by its synergistic interaction between LaFeO₃ and MgAl-LDH, the composite exhibits superior adsorption efficiency, with a maximum capacity of 833.3 mg-P per g, and excellent selectivity for phosphate ions at the optimal pH of 2. The removal process follows second-order kinetics and is well-described by both Langmuir and Freundlich isotherms, indicating a combination of physical and chemical adsorption mechanisms. Additionally, the composite maintains over 88% removal efficiency after five cycles, confirming its reusability, stability, and potential for practical applications. Overall, the MgAl-LDH/LaFeO₃ composite offers a promising, sustainable, and efficient approach for mitigating phosphate pollution and combating eutrophication in aquatic environments.

Conflicts of interest

There is no conflicts of interest to declare.

Data availability

The datasets supporting the findings of this study are available within the article. See DOI: **https://doi.org/10.1039/d5ra06299c**.

References

1 E. M. A. El-Monaem, M. M. A. El-Latif, A. S. Eltaweil and G. M. El-Subruiti, *Nano*, 2021, 16.
2 R. Saravanathamizhan and V. Perarasu, in *Wastewater Treatment*, Elsevier, 2021, pp. 103–136.
3 A. S. Eltaweil, E. M. Abd El-Monaem, H. M. Elshishini, H. G. El-Aqapa, M. Hosny, A. M. Abdelfatah, M. S. Ahmed, E. N. Hammad, G. M. El-Subruiti, M. Fawzy and A. M. Omer, *RSC Adv.*, 2022, **12**, 8228–8248.
4 M. A. Maia, G. L. Dotto, O. W. Perez-Lopez and M. Gutterres, *Environ. Technol.*, 2021, **42**, 3095–3105.
5 E. M. Abd El-Monaem, M. Hosny and A. S. Eltaweil, *Chem. Eng. Sci.*, 2024, **287**, 119707.
6 W. Wang, J. Zhou, G. Achari, J. Yu and W. Cai, *Colloids Surf., A*, 2014, **457**, 33–40.
7 D. Cordell and S. White, *Sustainability*, 2011, **3**, 2027–2049.
8 A. M. Omer, G. S. Elgarhy, G. M. El-Subruiti, E. M. Abd El-Monaem and A. S. Eltaweil, *Carbohydr. Polym.*, 2023, **311**, 120771, DOI: **10.1016/j.carbpol.2023.120771**.
9 Y. Cao, X. Wu, B. Li, X. Tang, X. Lin, P. Li, H. Chen, F. Huang, C. Wei and J. Wei, *Chemosphere*, 2023, **325**, 138378.
10 M. P. Bernardo and C. Ribeiro, *Mater. Res.*, 2018, **21**, e20171001.
11 L. Feng, Q. Zhang, F. Ji, L. Jiang, C. Liu, Q. Shen and Q. Liu, *Chem. Eng. J.*, 2022, **430**, 132754.
12 R. E. K. Billah, Z. Azoubi, E. A. López-Maldonado, H. Majdoubi, H. Lgaz, E. C. Lima, A. Shekhawat,

Y. Tamraoui, M. Agunaou and A. Soufiane, *ACS Omega*, 2023, **8**, 10051–10061.
13 H. M. Elshishini, G. M. El-Subruiti, Z. F. Ghatass, N. H. Farag and A. S. Eltaweil, *J. Water Process Eng.*, 2025, **69**, 106678, DOI: **10.1016/j.jwpe.2024.106678**.
14 C. Wang, Y. Wu, Y. Wang, L. Bai, H. Jiang and J. Yu, *Water Res.*, 2018, **137**, 173–183.
15 R. Mishra, Y.-M. Kim, J. Salafranca, S. K. Kim, S. H. Chang, A. Bhattacharya, D. D. Fong, S. J. Pennycook, S. T. Pantelides and A. Y. Borisevich, *Nano Lett.*, 2014, **14**, 2694–2701.
16 Y. Xu, S. Song, C. Li, B. Hong, D. Shi, J. Xu, Y. Han, H. Jin, D. Jin and X. Peng, *Mater. Chem. Phys.*, 2021, **267**, 124628.
17 K.-H. Goh, T.-T. Lim and Z. Dong, *Water Res.*, 2008, **42**, 1343–1368.
18 C. Novillo, D. Guaya, A. A.-P. Avendaño, C. Armijos, J. Cortina and I. Cota, *Fuel*, 2014, **138**, 72–79.
19 M. M. Hessien, G. A. Mersal, Q. Mohsen and D. Alosaimi, *J. Mater. Sci.: Mater. Electron.*, 2017, **28**, 4170–4178.
20 B. Yang, Y. Feng, Y. Yu, S. He, H. Liu, L. Xue and L. Yang, *Environ. Sci. Pollut. Res.*, 2019, **26**, 22010–22020.
21 J. Zhou, S. Yang, J. Yu and Z. Shu, *J. Hazard. Mater.*, 2011, **192**, 1114–1121.
22 B. R. Gevers, S. Naseem, A. Leuteritz and F. J. Labuschagné, *RSC Adv.*, 2019, **9**, 28262–28275.
23 L. Kong, Y. Tian, Z. Pang, X. Huang, M. Li, R. Yang, N. Li, J. Zhang and W. Zuo, *Chem. Eng. J.*, 2019, **371**, 893–902.
24 B. Yang, Y. Feng, Y. Yu, S. He, H. Liu, L. Xue and L. Yang, *Environ. Sci. Pollut. Res.*, 2019, **26**, 22010–22020.
25 R. Benhiti, A. Ait Ichou, A. Zaghloul, G. Carja, M. Zerbet, F. Sinan and M. Chiban, *J. Hazard. Mater.*, 2021, **6**, 16.
26 X. Qi, J. Zhou, Z. Yue, Z. Gui and L. Li, *Mater. Chem. Phys.*, 2003, **78**, 25–29.
27 Q. Cui, G. Jiao, J. Zheng, T. Wang, G. Wu and G. Li, *RSC Adv.*, 2019, **9**, 18641–18651.
28 H. M. Elshishini, G. M. Elsubruiti, Z. F. Ghatass and A. S. Eltaweil, *J. Solid State Chem.*, 2024, **335**, 124689, DOI: **10.1016/j.jssc.2024.124689**.
29 M. S. Ayoup, A. S. Eltaweil, A. M. Omer and E. M. Abd El-Monaem, *Int. J. Biol. Macromol.*, 2024, **281**, 136288, DOI: **10.1016/j.ijbiomac.2024.136288**.
30 A. S. Eltaweil, N. Mohamed Gaber, G. M. El-Subruiti and A. M. Omer, *J. Mol. Liq.*, 2024, **394**, 123716, DOI: **10.1016/j.molliq.2023.123716**.
31 F. Z. Mahjoubi, A. Khalidi, M. Abdennouri and N. Barka, *J. Taibah Univ. Sci.*, 2017, **11**, 90–100.
32 I. Palinko, P. Sipos, O. Berkesi and G. Varga, *J. Phys. Chem. C*, 2022, **126**, 15254–15262.
33 Bhojaraj, J. Arulraj, M. R. Kolinjavadi and M. Rajamathi, *ACS Omega*, 2019, **4**, 20072–20079.
34 L. D. Silva Neto, C. G. Anchieta, J. L. Duarte, L. Meili and J. T. Freire, *ACS Omega*, 2021, **6**, 21819–21829.
35 A. F. Morais, I. G. Silva, B. J. Ferreira, A. C. Teixeira, S. P. Sree, H. Terraschke, F. A. Garcia, E. Breynaert and D. Mustafa, *Chem. Commun.*, 2023, **59**, 13571–13574.
36 E. M. Abd El-Monaem, A. M. Omer and A. S. Eltaweil, *J. Polym. Environ.*, 2024, **32**, 2075–2090.

37 K. Bourikas, C. Kordulis and A. Lycourghiotis, *Adv. Colloid Interface Sci.*, 2006, **121**, 111–130.

38 S. Yu, X. Wang, Y. Liu, Z. Chen, Y. Wu, Y. Liu, H. Pang, G. Song, J. Chen and X. Wang, *Chem. Eng. J.*, 2019, **365**, 51–59.

39 Y. Uwamino, T. Ishizuka and H. Yamatera, *J. Electron Spectrosc. Relat. Phenom.*, 1984, **34**, 67–78.

40 Z. Wang, *et al.*, *Chemosphere*, 2016, **150**, 1–7.

41 J. Xie, Z. Wang, S. Lu, D. Wu, Z. Zhang and H. Kong, *Chem. Eng. J.*, 2014, **254**, 163–170.

42 M. Zhang, B. Gao, Y. Yao, Y. Xue and M. Inyang, *Chem. Eng. J.*, 2012, **210**, 26–32.

43 D. Jiang, B. Chu, Y. Amano and M. Machida, *Colloids Surf., A*, 2018, **558**, 429–437.

44 Z. Wang, D. Shen, F. Shen and T. Li, *Chemosphere*, 2016, **150**, 1–7.

45 S. Dong, Y. Wang, Y. Zhao, X. Zhou and H. Zheng, *Water Res.*, 2017, **126**, 433–441.

46 E. B. Azimi, A. Badiei and J. B. Ghasemi, *Appl. Surf. Sci.*, 2019, **469**, 236–245.

47 J. G. Catts and D. Langmuir, *Appl. Geochem.*, 1986, **1**, 255–264.

48 K. Hosni and E. Srasra, *Colloid J.*, 2010, **72**, 423–431.

49 T. M. Budnyak, M. Błachnio, A. Slabon, A. Jaworski, V. A. Tertykh, A. Deryło-Marczewska and A. W. Marczewski, *J. Phys. Chem. C*, 2020, **124**, 15312–15323.

50 J. Das, B. Patra, N. Baliarsingh and K. Parida, *Appl. Clay Sci.*, 2006, **32**, 252–260.

51 P. Koilraj, C. Jinesh and S. Kannan, *Application of Adsorbents for Water Pollution Control*, Bentham Science Publishers Ltd, Sharjah, UAE, 2012, pp. 153–237.

52 J. Zhang, J. Sun, Y. Liu, J. Wang and Y. Nie, *J. Water Process Eng.*, 2024, **65**, 105800.

53 D. Mustafa, B. Ibrahim and A. Erten, *Sci. Rep.*, 2024, **14**, 17765.

54 S. Chatterjee and S. H. Woo, *J. Hazard. Mater.*, 2009, **164**, 1012–1018.

55 M. N. Afridi, J. Lee and J.-O. Kim, *Desalin. Water Treat.*, 2019, **144**, 355–369.

56 K. Yang, L.-g. Yan, Y.-m. Yang, S.-j. Yu, R.-r. Shan, H.-q. Yu, B.-c. Zhu and B. Du, *Sep. Purif. Technol.*, 2014, **124**, 36–42.

57 K. Riahi, S. Chaabane and B. B. Thayer, *J. Saudi Chem. Soc.*, 2017, **21**, S143–S152.

58 R. Benhiti, A. Ait Ichou, A. Zaghloul, G. Carja, M. Zerbet, F. Sinan and M. Chiban, *Nanotechnol. Environ. Eng.*, 2021, **6**, 1–12.

59 K.-W. Jung, S. Lee and Y. J. Lee, *Bioresour. Technol.*, 2017, **245**, 751–759.

60 M. B. McBride, *Environna Ental Chemistry of So∥LS*, 1994.

61 C. Liu, M. Zhang, G. Pan, L. Lundehøj, U. G. Nielsen, Y. Shi and H. C. B. Hansen, *Appl. Clay Sci.*, 2019, **177**, 82–90.

62 R. Li, J. J. Wang, B. Zhou, M. K. Awasthi, A. Ali, Z. Zhang, L. A. Gaston, A. H. Lahori and A. Mahar, *Sci. Total Environ.*, 2016, **559**, 121–129.

63 Z. Lin and J. Chen, *Chemosphere*, 2021, **264**, 128551.

64 A. K. Khalil, F. Dweiri, I. W. Almanassra, A. Chatla and M. A. Atieh, *Sustainability*, 2022, **14**, 6991.

65 P. Karthikeyan and S. Meenakshi, *J. Mol. Liq.*, 2019, **296**, 111766.

66 F. Hu, M. Wang, X. Peng, F. Qiu, T. Zhang, H. Dai, Z. Liu and Z. Cao, *Colloids Surf., A*, 2018, **555**, 314–323.